


## Robust microstructure of self-aligning particles in a simple shear flow

Neeraj S. Borker *Sibley School of Mechanical and Aerospace Engineering, Cornell University, Ithaca, New York 14853, USA*Abraham D. Stroock and Donald L. Koch *Smith School of Chemical and Biomolecular Engineering, Cornell University, Ithaca, New York 14853, USA*

(Received 15 July 2023; accepted 11 March 2024; published 24 April 2024)

A self-aligning particle (SAP) attains a permanent orientation without application of external torques in a low Reynolds number simple shear flow in contrast with the continuous rotation exhibited by most rigid bodies including thin fibers and disks. SAPs align close to the fluid lamellae, and we characterize the robustness of this flow alignment to secondary disturbances such as perturbation to the shear flow, Brownian motion, interparticle interactions, or the presence of a wall using dynamic simulations of representative SAP geometries. The robustness of the flow alignment of SAPs at all concentrations generates highly aligned microstructures inaccessible to traditional particle suspensions.

DOI: [10.1103/PhysRevFluids.9.043301](https://doi.org/10.1103/PhysRevFluids.9.043301)

### I. INTRODUCTION

Self-aligning particles (SAPs) are defined as rigid bodies that attain an equilibrium orientation without applying any external forces or torques in a simple shear flow (SSF), which is a linear approximation to the pressure-driven flow found in many natural and industrial processes [1,2]. While most other high-aspect ratio rigid bodies, including fibers and disks, spend long times aligned near the flow-vorticity plane, the particles eventually perform a quick tumble (referred as the tumbling phase), repeating the align-tumble cycles continuously [3,4]. The large change in the particle orientation during the tumbling phase has the greatest impact on the orientational microstructure of the underlying suspensions, resulting in significant deviations from a perfectly flow-aligned state [5–7]. On the contrary, SAPs [4,8,9] permanently align close to the shear flow lamellae, and this could allow for material fabrication with nearly perfect anisotropy using existing processing-flow techniques like injection molding or casting. Permanent alignment of geometries described in [9] has been demonstrated in preliminary experiments [10].

Managing the orientation of individual particles can help to engineer functional materials with precise control over the mechanical, optical, or electrical properties of the final product [2,11–13]. For instance, SAPs embedded during the curing process can be used to fabricate lightweight materials with a layered microstructure for withstanding crack propagation [14,15]. Conducting SAPs could provide an easier route for making optical films with uniform planar conductivity desirable in electronics [16]. This study aims to advance our understanding of the behavior of SAP suspensions to realistic perturbations and lay a foundation for their use in these applications.

We compute the orientational microstructure of individual SAPs and then describe changes in the microstructure caused by perturbations to the imposed shear flow, Brownian motion, interparticle interactions, or a wall through dynamic simulations. Half the extent of the ring in its plane,  $R$ , and the shear rate of the SSF,  $\gamma$ , are used to nondimensionalize all properties of interest. The aspect ratio  $A \gg 1$  is defined as the ratio of  $2R$  and the extent of the ring along its axis of symmetry.

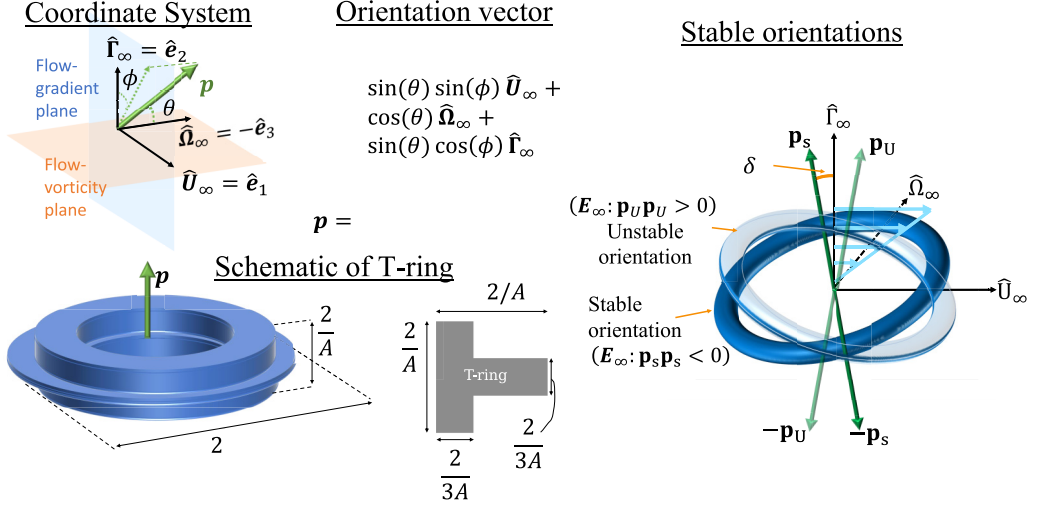


FIG. 1. Coordinate systems, schematic of a T ring, and the stable ( $\pm \mathbf{p}_S$ ) (solid ring) and unstable ( $\pm \mathbf{p}_U$ ) (translucent ring) nodes of the SAP. All distances are in nondimensional units.

## II. ISOLATED PARTICLE MICROSTRUCTURE

Rings with a blunt inner and sharper outer edge, such as the one shown in Fig. 1, can self-align without application of any external torques. SAPs when oriented near the flow-vorticity plane utilize the fluid pressure to generate an  $O(A^{-1})$  countervorticity rotation [8,9] that balances the  $O(A^{-2})$  shear stress-induced covorticity rotation experienced by all slender particles. The rate of change of orientation of the axis of symmetry,  $\mathbf{p}$ , equals

$$\dot{\mathbf{p}} = \boldsymbol{\omega}_\infty \times \mathbf{p} + \lambda (\mathbf{E}_\infty \cdot \mathbf{p} - \mathbf{E}_\infty : \mathbf{p}\mathbf{p}\mathbf{p}), \quad (1)$$

where  $\lambda$  is the rotation parameter that depends on the particle shape [3,4,8,9],  $\boldsymbol{\omega}_\infty = \nabla \times \mathbf{u}_\infty / 2$ ,  $\mathbf{E}_\infty = (\nabla \mathbf{u}_\infty + (\nabla \mathbf{u}_\infty)^T) / 2$  is the rate of strain tensor, and  $\mathbf{u}_\infty$  is the velocity field of the imposed SSF.  $\lambda$  for high aspect ratio rings is given by

$$\lambda = -1 + C_\lambda \frac{1}{\epsilon A^2} \left( 1 - \frac{3}{2} \epsilon \right) - \frac{C_\alpha}{A}, \quad (2)$$

where  $\epsilon = 1/\ln(8A) \ll 1$  is a small parameter arising in the slender-body-theory (SBT) treatment of the ring [17,18];  $C_\lambda > 0$  and  $C_\alpha$  are constants that depend only on the cross-sectional shape. A ring self-aligns only when  $C_\alpha > 0$ , and the magnitude of  $C_\alpha > 0$  quantifies the ease of alignment. A ring attains an equilibrium orientation  $\mathbf{p} = \pm \mathbf{p}_S = \pm(-\sin(\delta), \cos(\delta), 0)$  when  $\lambda \leq -1$ ,  $\delta = (1/2)\cos^{-1}(-1/\lambda)$  and rotates in periodic Jeffery orbits [3,4] with a time period  $T = 4\pi/\sqrt{1-\lambda^2} \approx 2\pi\delta_T^{-1}$  when  $-1 < \lambda < 0$ . Here  $\delta_T = \sqrt{(1+\lambda)/(1-\lambda)}$  is a measure of the average tilt of a tumbling ring during its periodic trajectory. Figure 2(a) shows the orientation trajectories of an  $A = 55$  torus for different initial conditions. These trajectories are periodic and termed Jeffery orbits. Figure 2(b) shows the orientation trajectories of an  $A = 55$  SAP with the shape illustrated in Fig. 1, for different initial conditions. All trajectories approach the stable nodes at  $\mathbf{p}_S$  and  $-\mathbf{p}_S$ .

The orientational dynamics described by Eq. (1) in the geometric space defined by  $A$  and  $C_\alpha/C_\lambda$  is constructed from boundary-element-method simulations [8,9] for rings with various cross sections as shown in Fig. 3 (symbols). The symbol color represents  $T$  relative to the time period of an equivalent torus ( $T_t$ ) for tumbling particles, and the magnitude of the equilibrium angle  $\delta$  for SAPs. The curve  $C_\alpha A^* = C_\lambda / [\ln(8A^*) - 3/2]$ , corresponding to  $\lambda = -1$ , represents the boundary

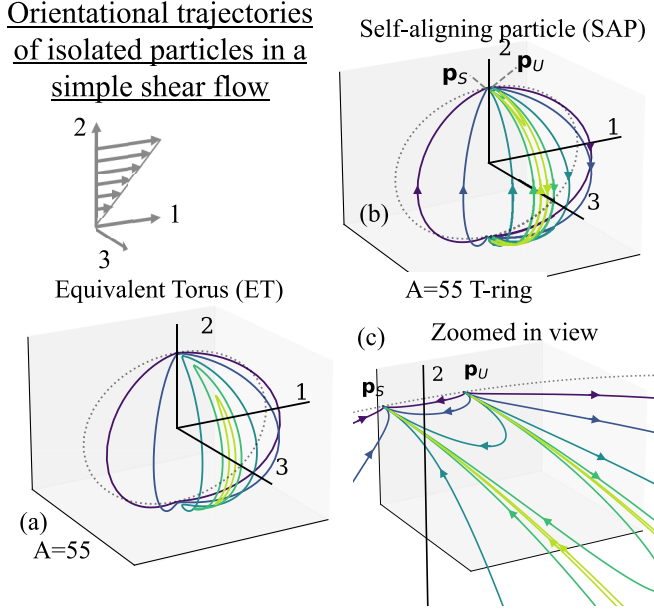


FIG. 2. Orientational trajectories of an isolated (a) Equivalent torus and (b) SAP of aspect ratio  $A = 55$ . (c) Orientation trajectories of an isolated SAP near the stable  $\mathbf{p}_s$  and unstable  $\mathbf{p}_u$  nodes.

between self-aligning and tumbling rings. A ring with a cross section with  $C_\alpha > 0$  rotates like an equivalent torus (ET) for  $\Delta A = A^* - A = O(1) > 0$ , rotates much slower than an ET for  $\Delta A \ll A^*$ , and self-aligns for  $A \geq A^*$ . Small changes in  $A$  near  $A^*$  drastically change the orientational dynamics of the particle and lead to sharp changes in the orientational microstructure of the underlying suspension. We use a family of T rings, shown in Fig. 1, as a model geometry to elucidate differences in suspension microstructure arising from the bifurcation in the orientation dynamics at  $A = A^*$ . T rings were also chosen due to accessibility to fabrication using multistep photolithography [19,20] and because  $A^*$  had a moderate value of 26. The divergence of  $T$  near  $A = A^*$  for T rings is shown in Fig. 4(a), and the value for an ET is shown for reference. The alignment angle  $\delta$  increases rapidly from zero near  $A = A^*$  to a peak value at  $A = 55$  and thereafter decreases slowly with increasing  $A$ . The qualitative trend of a diverging time period near  $A = A^*$  and a rapid increase in  $\delta$  near  $A = A^*$  followed by a slower decrease for larger  $A$  holds true for all rings with  $C_\alpha > 0$  as shown in Fig. 3.

The alignment of a ring relative to the flow-vorticity plane is quantified through a flow-alignment parameter  $k = k_0 + O(n) = (3/2)\langle 1 - p_2^2 \rangle_J$  shown in Fig. 4(b). Here  $n$  is nondimensional number density normalized by  $R^{-3}$ ; and  $\langle \cdot \rangle_J$  is the ensemble average taken over the steady-state orientation distribution determined by pairwise interactions or weak Brownian motion ( $D_r \ll \gamma \delta_T^3$ ) (both giving similar results [21]) for tumbling rings and described by the deviation from the equilibrium orientation for SAPs, i.e.,  $k_0 = (3/2)(1 - p_{S,2}^2)$ . Here  $D_r$  is the rotary diffusivity of the ring.  $k$  equals one for an isotropic suspension and zero if all particles are aligned in the flow-vorticity plane. Although an ET remains aligned near the flow-vorticity plane for long  $O(\delta_T^{-1}) = O(A)$  times, the short  $O(1)$  tumbling phase has the greatest contribution to  $k$ , making  $k$  proportional to the  $O(A^{-1})$  tumbling frequency [5]. The value of  $k$  for tumbling T rings away from  $A = A^*$  is similar to  $k$  for ETs.  $k$  sharply drops for tumbling T rings near  $A = A^*$  suggesting greater flow alignment caused by the rapid increase in the rotational time period shown in Fig. 4(a). SAPs are always aligned near the flow-vorticity plane and therefore possess a much smaller value of  $k_0 = (3/2)\sin^2(\delta) = O(\Delta A A^{-3}) \gg \delta_T = O(A^{-1})$  compared to an ET. The flow-alignment parameter of equivalent fibers,  $k_{0f} = (3/2)\langle 1 - p_1^2 \rangle_J = O(A^{-1})$ , is also shown in Fig. 4(b) [22] to demonstrate that SAPs also have

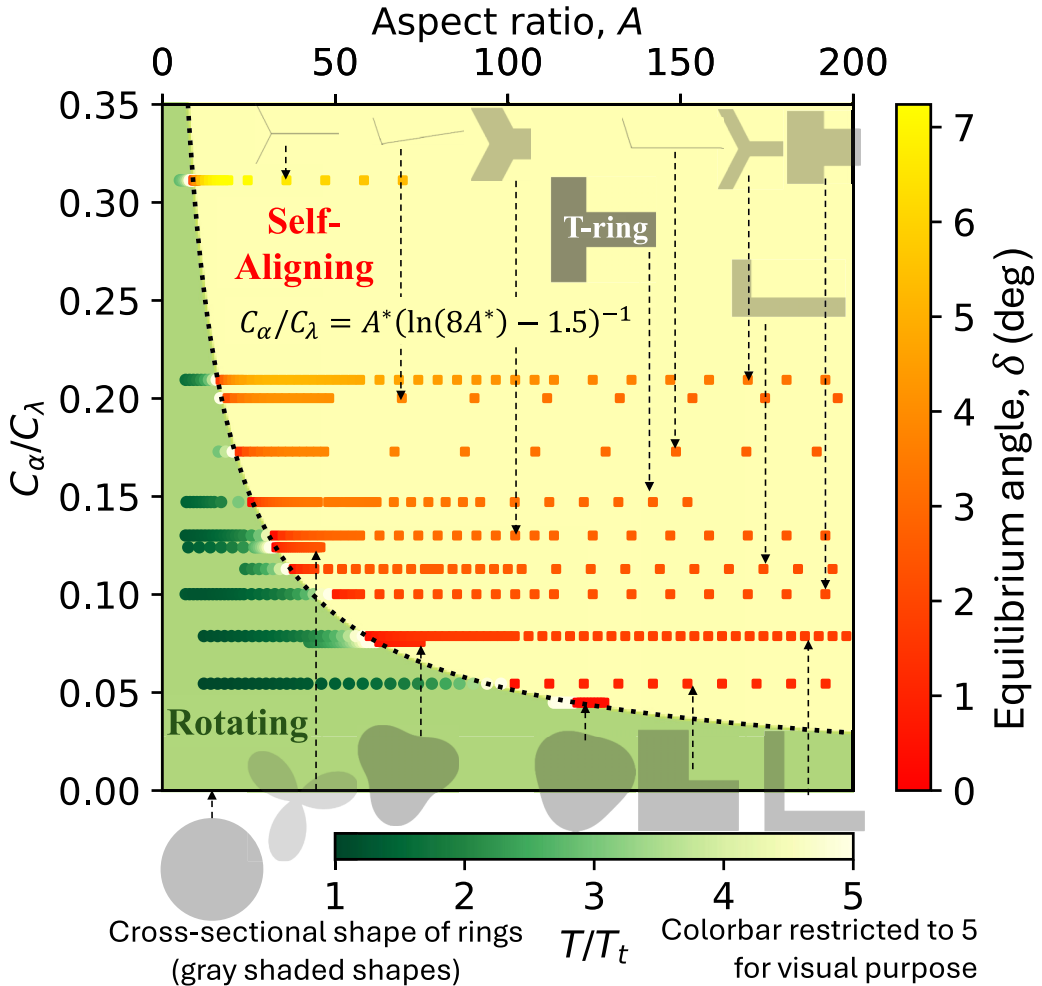


FIG. 3. State of the orientational dynamics of rings in the  $(A, C_\alpha/C_\lambda)$  space. Color represents  $T/T_t$  for tumbling rings and the equilibrium angle  $\delta$  for SAPs. Symbols with the same value of  $C_\alpha/C_\lambda$  correspond to rings with the same cross-sectional shape. Cross sections of the rings are also shown with transparent gray background. These cross sections are illustrated such that the axis of symmetry of each ring is on the left side of the cross section.

better flow alignment than fibers. By virtue of their permanent alignment, SAPs were found to have the highest degree of flow alignment among all slender-particle geometries of the same size and aspect ratio.

Recall that a SAP also has an unstable node  $\mathbf{p}_U$ , i.e., a ring's orientation rotates away from  $\mathbf{p}_U$  when it is in close proximity. The unstable node is at an angular separation of  $2\delta = O(A^{-1}\sqrt{\Delta A/A})$  from the stable node  $\mathbf{p}_S$  as shown in Fig. 2(c). If  $\phi$  becomes larger than  $\delta$ , then  $\mathbf{p}$  will move towards the stable node  $-\mathbf{p}_S$  and cause the SAP to tumble, disturbing the microstructure. This suggests the possibility that small disturbances, such as those induced through perturbations to the SSF, Brownian motion, interparticle interactions, or walls, could rotate a SAP towards its unstable node. We now describe the impact of each of these secondary perturbations on the flow alignment of SAPs.

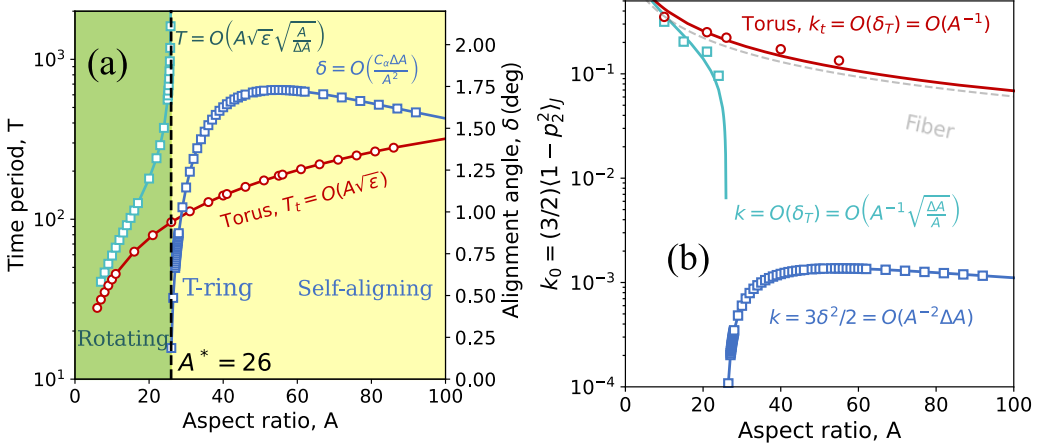


FIG. 4. Isolated particle properties (a)  $T$  for tori and T rings ( $A < A^*$ ) and  $\delta$  for T rings ( $A \geq A^*$ ) as a function of  $A$ . (b)  $k_0$  as a function of  $A$  for T rings, tori, and fibers. All order of magnitude scalings are derived from the SBT treatment of rings.

### III. PERTURBATIONS TO SIMPLE SHEAR FLOW (SSF)

We studied the impact of time-varying fluctuations on each component of  $\omega_\infty$  and  $\mathbf{E}_\infty$ , with the perturbations taking the form  $\varepsilon_s \hat{f}_s(t)/2$  with the initial condition  $\mathbf{p} = \mathbf{p}_S$ . Here  $\hat{f}_s(t) = \sin(2\pi \zeta_s t + d_s)$ ; and  $\varepsilon_s$ ,  $\zeta_s$ , and  $d_s$  are the amplitude, frequency, and phase angle of the perturbation, respectively. The subscript  $s \in \{\omega_1, \omega_2, \omega_3\} \cup \{E_{11}, E_{12}, E_{13}, E_{22}, E_{23}\}$  corresponds to the component of the vorticity vector and straining tensor, respectively. The disturbance to the microstructure was quantified by the change in the orientation parameter  $k_\varepsilon = (3/2)(p_{S,2}^2 - \langle p_2^2 \rangle_\varepsilon)$ , where  $\langle \cdot \rangle_\varepsilon$  is the time average of the orientation moments over a long period of time.

The perturbation to  $\omega_3$  causes a small oscillatory change in the magnitude of the vorticity vector of the SSF and causes rotation of  $\mathbf{p}$  in the flow-gradient plane. Figure 5(a) shows the value of  $k_\varepsilon/\delta^2$  (color/contour) as a function of  $\varepsilon_{\omega_3}$  and  $\zeta_{\omega_3}$  for an  $A = 55$  SAP. The orientational dynamics can be divided into two qualitatively different regimes in which (1)  $\mathbf{p}$  wobbles around  $\mathbf{p}_S$  causing an  $O(\delta^2)$  change in  $k_\varepsilon$  (dark region) and (2)  $\mathbf{p}$  tumbles in the flow-gradient plane after being pushed near the unstable node  $\mathbf{p}_U$  causing an  $O(1)$  change in  $k_\varepsilon$  and greatly disturbing the microstructure (light region). The critical amplitude of the perturbation separating these two regimes can be obtained analytically by solving Eq. (1) in the vicinity of the equilibrium orientation using rescaled variables for time  $\tau = t\delta$ , azimuthal angle  $\eta = \phi/\delta = O(1)$ , and polar angle  $\chi = (\theta - \pi/2)$ . The evolution equations for  $\eta$  and  $\chi$  are given by

$$\begin{aligned} \frac{d\eta}{d\tau} = & \eta^2 - 1 - \frac{1}{2\delta^2}(\varepsilon_{\omega_3}\hat{f}_{\omega_3} + \varepsilon_{E_{12}}\hat{f}_{E_{12}}) + \chi \frac{1}{2\delta^2}(\varepsilon_{\omega_2}\hat{f}_{\omega_2} - \varepsilon_{E_{13}}\hat{f}_{E_{13}}) \\ & - \eta \frac{1}{2\delta}(\varepsilon_{E_{11}}\hat{f}_{E_{11}} - \varepsilon_{E_{22}}\hat{f}_{E_{22}}) + \chi \eta \frac{1}{2\delta}(\varepsilon_{\omega_1}\hat{f}_{\omega_1} + \varepsilon_{E_{23}}\hat{f}_{E_{23}}), \end{aligned} \quad (3)$$

$$\begin{aligned} \frac{d\chi}{d\tau} = & \chi \eta + \frac{1}{2\delta}(\varepsilon_{\omega_1}\hat{f}_{\omega_1} - \varepsilon_{E_{23}}\hat{f}_{E_{23}}) - \frac{\eta}{2}(\varepsilon_{\omega_2}\hat{f}_{\omega_2} + \varepsilon_{E_{13}}\hat{f}_{E_{13}}) \\ & \times \frac{\chi}{2}(\varepsilon_{E_{11}}\hat{f}_{E_{11}} + 2\varepsilon_{E_{22}}\hat{f}_{E_{22}}) + \chi \eta \varepsilon_{E_{12}}\hat{f}_{E_{12}} + \chi^2 \varepsilon_{E_{23}}\hat{f}_{E_{23}} \\ & + \eta \chi^2 \varepsilon_{E_{13}}\hat{f}_{E_{13}} + \frac{\delta}{2} \eta^2 \chi \varepsilon_{E_{11}}\hat{f}_{E_{11}} - \chi^3 (\varepsilon_{E_{11}}\hat{f}_{E_{11}} + \varepsilon_{E_{22}}\hat{f}_{E_{22}}). \end{aligned} \quad (4)$$

Equation (3) suggests that SAPs will not tumble from perturbations to  $\omega_3$  at all frequencies if  $\varepsilon_{\omega_3} < 2\delta^2$ , shown by the dotted line in Fig. 5(a). Linear stability analysis of Eq. (3) around  $\eta = -1$

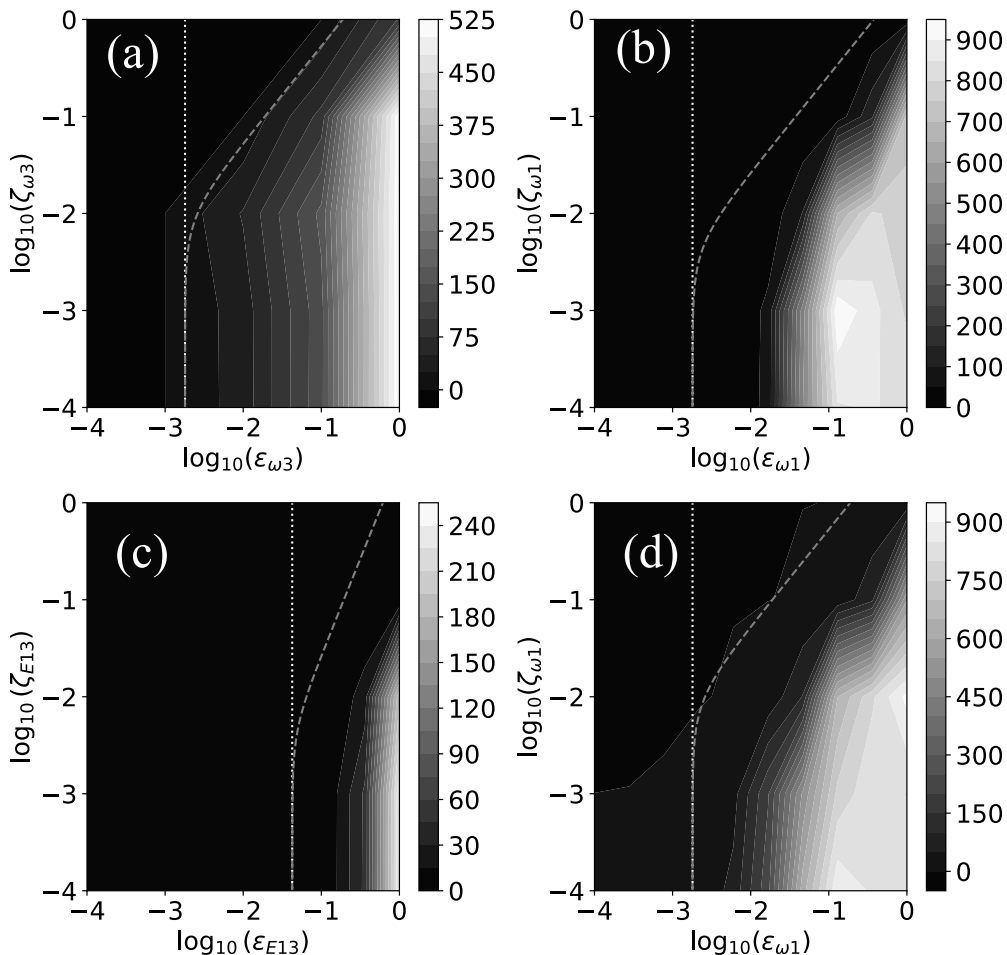


FIG. 5. Effect of perturbations to the SSF. Contours of  $k_e/\delta^2$  as a function of varying amplitude and frequency of the perturbation for different modes: (a)  $(\varepsilon_{\omega_3}, \zeta_{\omega_3})$ , (b)  $(\varepsilon_{\omega_1}, \zeta_{\omega_1})$ , (c)  $(\varepsilon_{E13}, \zeta_{E13})$ , and (d)  $(\varepsilon_{\omega_1}, \zeta_{\omega_1})$  with  $(\varepsilon_{\omega_3}, \zeta_{\omega_3}, d_{\omega_3}) = (\delta^2, 0.1\delta^2, 0.1\delta)$ .

provides the condition for the critical perturbation as  $\varepsilon_{\omega_3} \ll 8\delta^2[1 + (\pi\zeta_{\omega_3}/\delta)^2]^{1/2}$  (see Section S5 in [23] for details). Linear stability analysis provides only the qualitative dependence of the critical  $\varepsilon_{\omega_3}$  on  $\zeta_3$  because the analysis ignores the existence of an unstable node at  $\eta = 1$  [29]. The dashed curve in Fig. 5(a) is given by  $\varepsilon_{\omega_3} = 2\delta^2[1 + (\pi\zeta_{\omega_3}/\delta)^2]^{1/2}$ , where the functional dependence on  $\zeta_{\omega_3}$  was taken from the prediction of the linear stability analysis and the constant was obtained from the global stability condition described earlier, valid as  $\zeta_{\omega_3} \rightarrow 0$ . The above condition is also consistent with numerical simulations which suggest that SAPs are more stable to higher frequency perturbations.

Figure 6 shows the orientational trajectory of a  $A = 55$  SAP (solid curve) in the  $(\phi, \theta)$  plane at different times for  $\zeta_{\omega_3}$  being near the critical amplitude value,  $\varepsilon_{\omega_3} = 0.95 \times 2\delta^2\sqrt{1 + (\pi\zeta_{\omega_3}/\delta)^2} \approx 1.8 \times 10^{-3}$ , and  $\zeta_{\omega_3} = 10^{-2}\delta$  and  $d_{\omega_3} = 0.0$ . The orientational velocity field  $(\dot{\phi}, \dot{\theta})$  is also shown (vectors). The orientation (x) moves from the stable node (o) towards the unstable node ( $\square$ ) of the unperturbed flow at  $t = 0$ . The stable and unstable nodes of the perturbed flow also oscillate, moving closer to each other [Fig. 6(a)] and moving away from each other [Fig. 6(c)]. Figure 6(b) corresponds to the state of minimum separation between the stable and

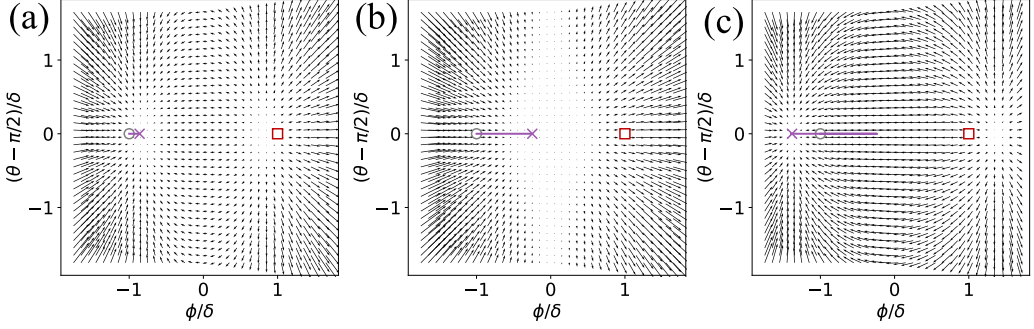


FIG. 6. Orientational trajectory (solid curve) of a  $A = 55$  SAP in the  $(\phi-\theta)$  plane for  $\varepsilon_{\omega 3} = 1.05\sqrt{2\delta^2[1 + (\pi\zeta_{\omega 3}/\delta)^2]} \approx 1.8 \times 10^{-3}$ ,  $\zeta_{\omega 3} = 10^{-2}\delta$  and  $d_{\omega 3} = 0.0$  at times (a)  $t = 0.05\zeta_{\omega 3}^{-1}$ , (b)  $t = 0.25\zeta_{\omega 3}^{-1}$ , and (c)  $t = 0.8\zeta_{\omega 3}^{-1}$ . Vectors represent the orientational velocity field  $(\dot{\phi}, \dot{\theta})$ , and symbols represent: stable node ( $\circ$ ), unstable node ( $\square$ ), and position at the given time ( $\times$ ).

unstable nodes for this perturbation. Supplemental Movie 1 shows the animation of this wobbling trajectory in the  $(\phi, \theta)$  plane. For higher perturbation frequencies, i.e.,  $\zeta_{\omega 3} \geq O(\delta)$ , the amplitude of the wobbling motion decreases (see Supplemental Movie 2). For amplitudes higher than the critical value, the stable and unstable nodes annihilate each other for a period of time during which the particle tumbles towards the stable node located at  $-\mathbf{p}_S$  (see Supplemental Movie 3). The value of  $k_e/\delta^2$  as a function of the amplitude and frequency of perturbations to  $E_{12}$  component of the straining tensor has a similar behavior [see Fig. S2(a) in the Supplemental Material [23]].

Perturbation to  $\omega_1$  (or  $E_{23}$ ) causes  $\mathbf{p}$  to rotate close to the gradient-vorticity plane of the SSF. SAPs can sustain  $O(1)$  changes in  $\theta$  without  $\phi$  ever approaching the value at the unstable node,  $\delta$ , as described by the trajectory of the particle in the  $(\phi, \theta)$  space shown in Fig. S3 of the Supplemental Material [23]. The phase diagram of  $d\eta/d\tau$  and  $\eta$  described by Eq. (3) [see Eq. (S5.8) of the Supplemental Material [23]] also indicates the presence of a stable node that oscillates around  $\eta = -1$ . Although the SAP does not tumble by crossing the unstable node, the  $O(1)$  wobbling amplitudes could disturb the microstructure of SAPs. This is qualitatively different from the effect of perturbations to  $\omega_3$  wherein a tumbling event was necessary to disturb the microstructure. The dependence of  $k_e/\delta^2$  on the frequency and amplitude of the oscillation is shown in Fig. 5(b). Linearizing Eqs. (3) and (4) around  $\eta = -1$  suggests that amplitudes of the oscillation satisfying  $\varepsilon_{\omega 1} \ll 2\delta^2[1 + (\pi\zeta_{\omega 1}/\delta)^2]^{1/2}$  ensure that the wobbling in the  $\theta$  direction is  $O(\delta)$  and the microstructure changes remain small. The variation of  $k_e/\delta^2$  due to perturbation to  $E_{23}$  is also similar and is shown in Fig. S2(b) of the Supplemental Material [23].

The perturbation to  $\omega_2$  drives rotation of  $\mathbf{p}$  around the gradient axis. Although a high enough value of  $\varepsilon_{\omega 2}$  can drive  $\phi$  to be larger than  $\delta$ , causing  $\mathbf{p}$  to move past the unstable node, the rotational motion curves  $\mathbf{p}$  back towards the stable node. The orientation trajectory and the velocity field  $(\dot{\phi}, \dot{\theta})$  shown in Fig. S4 of the Supplemental Material [23] describe this behavior.  $k_e/\delta^2$  as a function of  $\varepsilon_{\omega 2}$  and  $\zeta_{\omega 2}$  is shown in Fig. S2(c) of the Supplemental Material [23], which suggests that a SAP is stable to large perturbations to  $\varepsilon_{\omega 2}$ . The perturbation to  $E_{13}$  drives an extensional flow which causes  $\mathbf{p}$  to move towards the extensional axis of the perturbed flow field.  $\mathbf{p}$  oscillates with the change in the magnitude of the perturbation as shown by a sample trajectory in Fig. S5 of the Supplemental Material [23]. The amplitude of the wobbling driven by perturbation to  $E_{13}$  can cause a large change in  $k_e/\delta^2$  as shown by its variation with  $\varepsilon_{E_{13}}$  and  $\zeta_{E_{13}}$  in Fig. 5(c). Solution of Eqs. (3) and (4), such that  $|\eta + 1| \ll 1$  and  $\chi = O(\delta)$ , provides the condition that  $\varepsilon_{E_{13}} \ll \sqrt{2}\delta[1 + (2\pi\zeta_{\omega 3}/\delta)^2]^{1/2}$ . Notice that the amplitude of perturbations to  $E_{13}$  needs to be smaller than  $O(\delta)$  rather than  $O(\delta^2)$  described for the previous two perturbations. Numerical simulations indicate that SAPs retained their equilibrium orientation if  $\varepsilon_{\omega 3} < O(\delta^2)$ ,  $\varepsilon_{E_{12}} < O(\delta^2)$ ,  $\varepsilon_{\omega 1} < O(\delta)$ ,  $\varepsilon_{E_{23}} < O(\delta)$ , and



$\varepsilon_{E12} < O(\delta)$ . Figure 5(d) shows  $k_\varepsilon$  as a function of  $\varepsilon_{\omega 1}$  and  $\zeta_{\omega 1}$  for  $(\varepsilon_{\omega 3}, \zeta_{\omega 3}, d_{\omega 3}) = (\delta^2, 0.1\delta^2, 0.1\delta)$ , and other modes having zero amplitude.

#### IV. BROWNIAN MOTION

The randomizing effect of rotary Brownian motion competes with the flow-aligning effect of the SSF, and the relative strength is quantified through the Péclet number  $\text{Pe} = \gamma/D_r$ . Brownian dynamics (BD) simulations [30,31] of an  $A = 55$  T ring were used to study the differences between Brownian SAPs and ETs. This SAP has the highest value of  $\delta$  and thus the greatest resistance to Brownian motion. The motion of  $\mathbf{p}$  in the flow-gradient plane ( $\theta = \pi/2$ ), i.e., the change in the azimuthal angle  $\phi$ , provides a framework to qualitatively understand the influence of Brownian motion on a SAP.  $\mathbf{p}$  should not move past the unstable node if the diffusive flux is much smaller than the convective flux for  $\phi = O(\delta)$ . This condition is satisfied for  $\text{Pe} \gg \delta^{-3}$  as seen from the one-dimensional Fokker-Plank equation for  $P(\phi)$ , the steady-state probability density function of  $\phi$  [22,32]. The one-dimensional Fokker-Plank equation for the probability density  $P_\phi$  for the particle having an azimuthal angle  $\phi$  is given by

$$\frac{\partial P_\phi}{\partial t} + \frac{d}{d\phi} \left( \dot{\phi}_J P_\phi - \frac{1}{\text{Pe}} \frac{dP_\phi}{d\phi} \right) = 0, \quad (5)$$

where  $\dot{\phi}_J = (1/2)[1 + \lambda \cos(2\phi)]$  is obtained from the solution of Eq. (1). The steady-state orientation distribution  $P = \lim_{t \rightarrow \infty} P_\phi$  for SAPs with  $\text{Pe} \gg \delta^{-3}$  can be obtained by asymptotically matching  $P$  from an outer region where  $\phi = O(1)$  and an inner region where  $\phi = O(\delta)$ . Following the procedure in Petrich *et al.* [33], the uniformly valid solution is given by

$$P = \frac{C_o}{\hat{D}\delta^2} \exp \left[ \frac{1}{\hat{D}} \left( \frac{\phi^3}{3\delta^3} - \frac{\phi}{\delta} \right) \right] \int_{\phi/\delta}^{\infty} dx' \exp \left[ -\frac{1}{\hat{D}} \left( \frac{x'^3}{3} - x' \right) \right] + \frac{2C_o}{1 + \lambda \cos(2\phi)} - \frac{C_o}{\phi^2 - \delta^2}, \quad (6)$$

where  $\hat{D} = \text{Pe}^{-1}\delta^{-3}$  and  $C_o$  is a constant obtained by the normalization condition,  $\int_{-\pi/2}^{\pi/2} d\phi P = (1/2)$  (see section (S3) of the Supplemental Material [23] for derivation).

The shape of  $P(\phi)$  is shown in Fig. 7(a) at different  $\text{Pe}$ , where the thin dark lines are the semianalytical solution given by Eq. (6) and the thick transparent lines are the full-BD simulation results. Figure 7(b) shows the flow-alignment parameter  $k_0$  as a function of the shear rate through  $\text{Pe}$ .  $k_0$  equals  $(3/2)\delta^2$  for  $\text{Pe} \gg \delta^{-3} = 3.7 \times 10^4$ , and in this flow-aligned regime there is a clear distinction between the microstructure of suspensions of SAPs and ETs. For these high  $\text{Pe}$  values,  $\mathbf{p}$  of a SAP wobbles around  $\mathbf{p}_S$  as evident from the probability distribution (red line) in Fig. 7(a), and Brownian motion is too weak to induce any noticeable tumbles. With decreasing  $\text{Pe} = O(\delta^{-3})$ , as seen from Fig. 7(a), the dynamics transitions from a state of wobbling around  $\mathbf{p}_S$  at  $\text{Pe} = 10^5$  (green) to a state of noticeable flips ( $\text{Pe} = 10^4$ ) (violet) wherein Brownian kicks are strong enough to move  $\mathbf{p}$  beyond  $\mathbf{p}_U$ . In this flow regime, a SAP still retains greater alignment than an ET because of the stabilizing angular velocity  $\dot{\phi} = \phi^2 - \delta^2$  provided by the SSF when  $\mathbf{p}$  is close to the gradient direction, i.e.,  $|\phi| \ll 1$ . This can be seen from the probability distribution for SAPs and ETs at the same  $\text{Pe}$  as shown in Fig. 7(c). SAPs at  $\text{Pe} = 10^4$  (green curve) remain significantly more aligned than ETs at the same  $\text{Pe}$  (gray curve). The rotational period of SAPs also changes by three orders of magnitude in this flow regime as shown in Fig. 7(d). For lower shear rates with  $\text{Pe} \ll \delta^{-3}$ , the self-aligning behavior of a SAP is lost and the orientational structures of SAP and ET suspensions are nearly identical. Thus, SAPs provide greater resistance to Brownian motion than ETs above a critical  $\text{Pe} = O(\delta^{-3})$  for geometries studied here. In dimensional terms, a  $A = 55$  T ring with a  $1 \mu\text{m}$  radius will retain its self-alignment in a viscous fluid like glycerin ( $1 \text{ Pa s}$ ) for shear rates larger than  $47 \text{ s}^{-1}$  corresponding to  $\text{Pe} = 10^5$  [see Eq. (S3.7) in the Supplemental Material]. For the special case of  $A = A^*$ ,  $k_0$  decreases to zero as  $\text{Pe}^{-1/3}$  for  $\text{Pe} \gg 1$ , while geometries away from  $A = A^*$  have a behavior similar to the  $A = 55$  SAP.



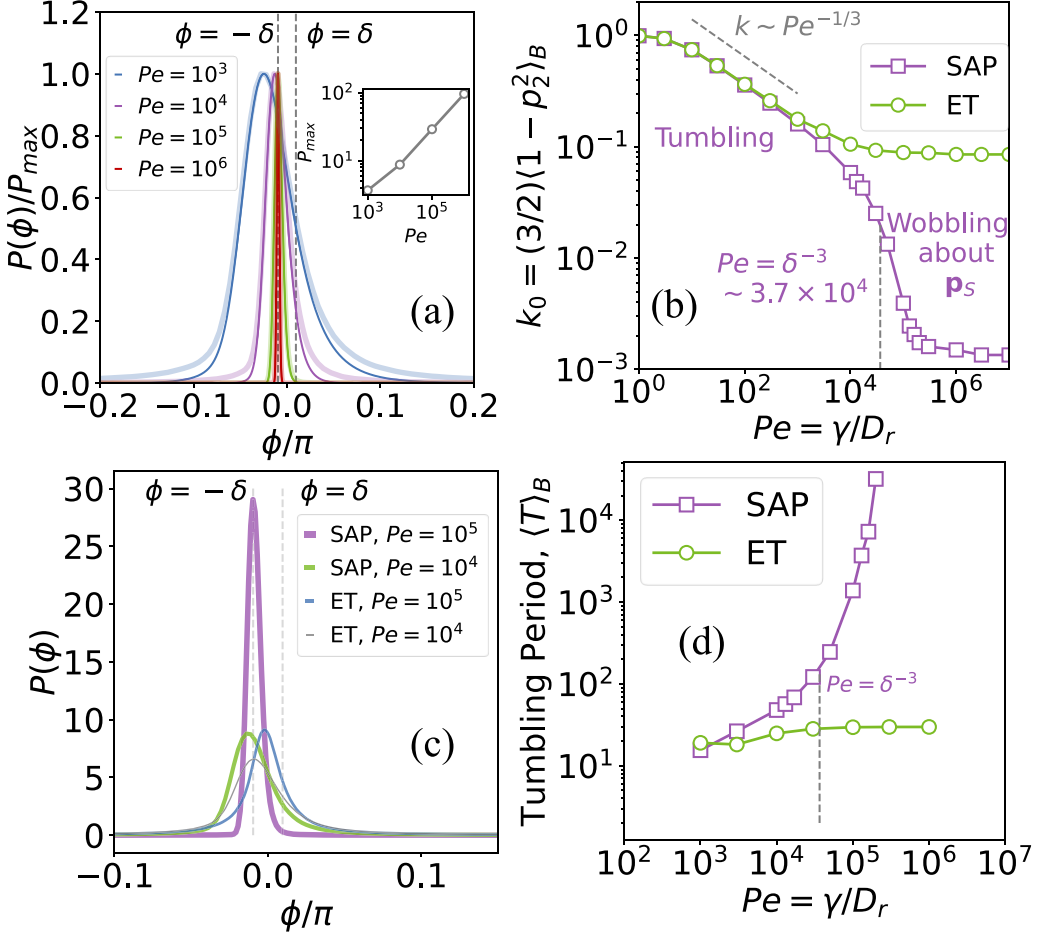


FIG. 7. Brownian motion effects. (a)  $P$ , the probability distribution function of  $\phi$ , for an  $A = 55$  SAP at various  $Pe$  using theory (thin line) and BD simulations (thick translucent line); inset shows the peak value of  $P$ ,  $P_{\max}$  as a function of  $Pe$ . (b) Flow-alignment parameter,  $k_0$  as a function of  $Pe$  for SAPs and ETs with  $A = 55$ . (c)  $P$  for a SAP and an ET of  $A = 55$  at  $Pe = 10^4$  and  $Pe = 10^5$ . (d) Tumbling period as a function of  $Pe$  for SAPs and ETs with  $A = 55$ .

## V. PAIRWISE INTERACTIONS BETWEEN SAPs

Permanent alignment of non-Brownian SAPs can be disturbed by interactions with other particles in the suspension, and this is captured using slender-body theory (SBT) [18,34] (see section S1 of the Supplemental Material [23] for a brief summary of the numerical implementation). SBT has been used to predict the microstructure in fiber suspensions [5,35–37] and has also recently been used to analyze interactions of tumbling rings [21]. Mechanical contact of tumbling rings which leads to an  $\delta_T = O(A^{-1})$  mean-squared change in  $\mathbf{p}$  is crucial, in addition to hydrodynamic interactions (HIs), in establishing the orientational structure even at dilute concentrations [21]. However, in a suspension of SAPs the  $O(\delta^2) = O(\Delta A A^{-3})$  collision frequency is so small that mechanical contacts have little contribution to changes in  $\mathbf{p}$  compared to HIs. Figure 8(a) shows the collision frequency,  $\beta_c$  of SAPs and ETs as a function of their aspect ratio. This confirms our assertion that particle collisions are rare in a suspension of SAPs compared to a suspension of ETs, and SAPs mainly have purely hydrodynamic interactions. The scaling of  $\beta_c$  for SAPs is obtained from the ideal-collision

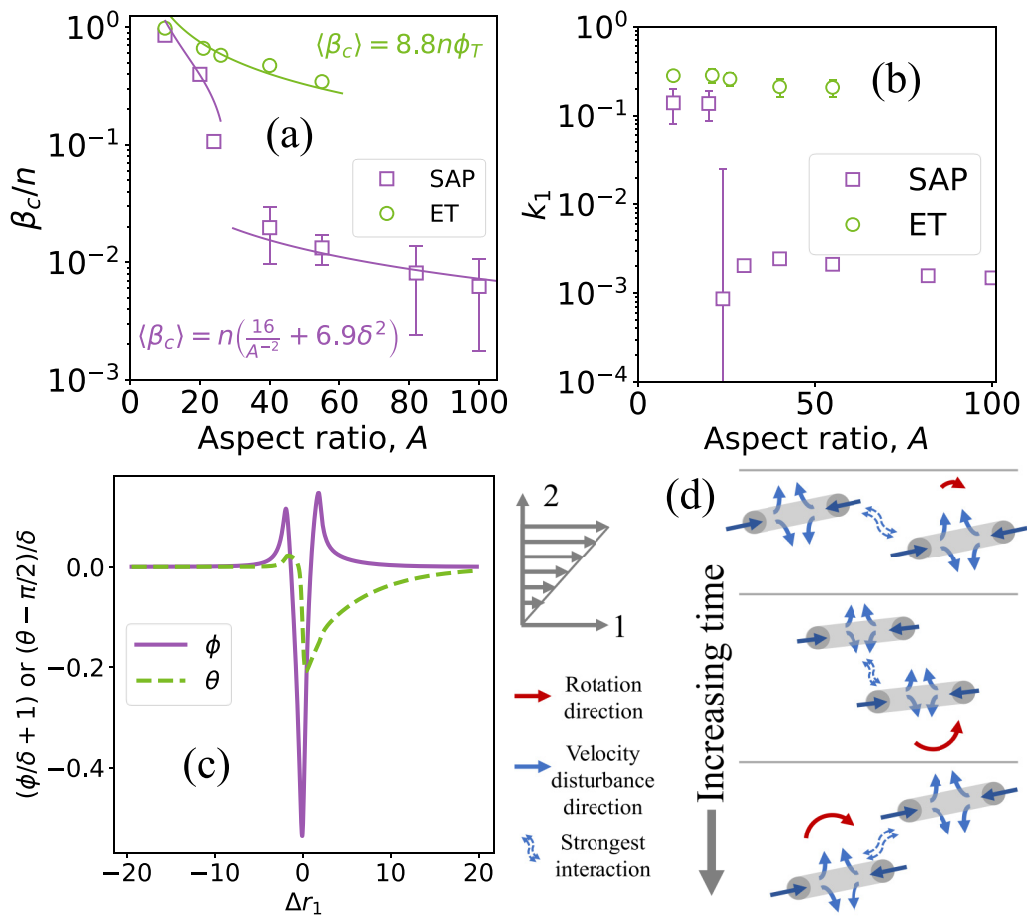


FIG. 8. Pairwise interactions (PIs). (a) Collision frequency,  $\langle\beta_c\rangle$ , and (b) effect of PIs on the orientational dispersion  $k_1$ , as a function of  $A$ . (c)  $\phi$  and  $\theta$  of a SAP as a function of  $\Delta r_1$  during an interaction with another SAP initially separated with  $\Delta r_1 = 10^3$ ,  $\Delta r_2 = 0.15$ ,  $\Delta r_3 = -0.13$ . (d) Schematic of hydrodynamic interactions of two SAPs in shear flow explaining the shape of the  $\phi$  trajectory in (c).

cross section in the gradient vorticity plane [38] and the scaling for tumbling particles is available [21]. Thus, SAPs mainly have weak HIs driven by the  $O(\epsilon\delta)$  velocity disturbance produced by a neighboring SAP, where the scaling is derived from SBT [34]. This leads to  $O(\epsilon\delta)$  changes in  $\mathbf{p}$  during each pairwise interaction (PI), and this displacement is much smaller than the angular separation between the stable and unstable nodes,  $2\delta$ . Therefore, flow alignment of SAPs is expected to be retained even with HIs, and this was confirmed by dynamic PI simulations of SAPs. We consider the  $O(\epsilon)$  change in the linear and angular velocity, and the  $O(\epsilon^2)$  change in the force distribution on a SAP due to the  $O(\epsilon)$  velocity disturbance generated by a neighboring SAP. A brief description of the simulation strategy is provided in section S1 of the Supplemental Material [23], and all details can be found in Sec. 2 of Borker and Koch [21].

Figure 8(b) shows the variation  $k - k_0 = nk_1 + O(n^2) = -(3/2)\langle p_2^2 - p_{J,2}^2 \rangle$ , with  $A$ , where  $\langle \cdot \rangle$  represents the ensemble average over all possible realizations of PIs and  $\mathbf{p}_J$  represents the Jeffery trajectory of isolated particles for tumbling rings [3,4] while  $\mathbf{p}_J = \mathbf{p}_S$  for SAPs. The magnitude of  $nk_1$  quantifies deviations in the orientational microstructure during PIs, and a positive  $k_1$  indicates degradation in flow alignment.  $k_1$  for T rings with  $A < A^*$  is similar to the  $O(A^{-1})$  value for

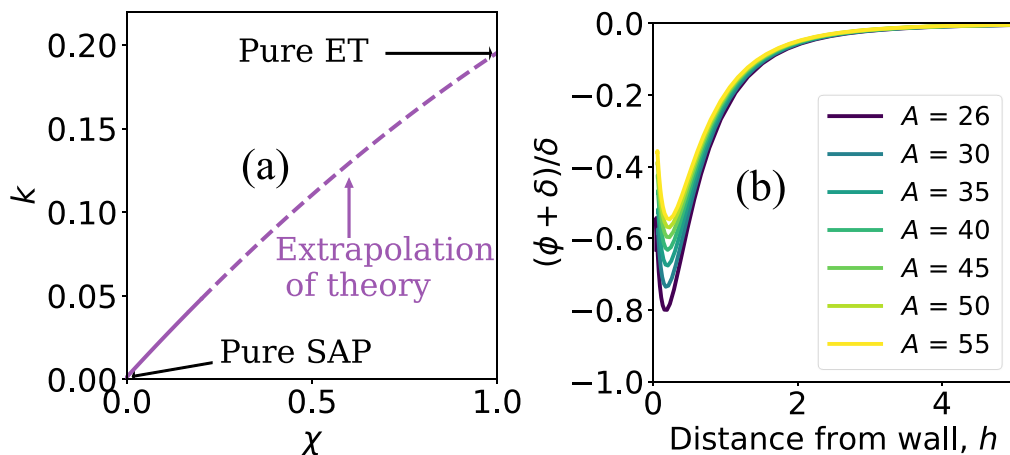


FIG. 9. Impact of tumbling impurities and wall. (a)  $k$  in a SAP-ET mixture as a function of  $\chi$  at  $n = 0.1$  for  $A = 40$  particles. (b)  $(\phi + \delta)/\delta$  as a function of  $h$ .

ETs, wherein major contributions arise from  $O(1)$  changes in  $\mathbf{p}$  during the  $O(nA^{-1})$  times when particles make mechanical contact [21]. SAPs, which interact through weak HIs, have a much smaller  $k_1 = O(\epsilon^2\delta^2) = O(\epsilon^2|\Delta A|A^{-3})$  than ETs. SAPs were found to only wobble around their equilibrium orientation due to PIs with other SAPs in the suspension. Figure 8(c) shows this wobbling motion through the variation of  $\phi$  and  $\theta$  as a function of the relative position of the particles in the flow direction  $\Delta r_1$ . The initial separations in the gradient and vorticity directions were  $\Delta r_2 = 0.15$  and  $\Delta r_3 = -0.13$ , respectively. The shape of the change in  $\phi$  can be explained from the qualitative nature of the velocity disturbances generated by the two particles shown by the schematic in Fig. 8(d). A SAP pulls fluid in the plane of the ring and pushes fluid out along its axis of symmetry [21] [see Fig. S1(b) of the Supplemental Material [23]]. As the particles approach each other, HIs between the nearest ends of the rings should induce a covorticity rotation as shown in Fig. 8(d). As the particles pass across each other in the flow direction, the nature of the hydrodynamic interaction changes and HIs should cause a countervorticity rotation. As the particles start moving apart, the nearest ends of the rings have the strongest interactions causing a covorticity rotation whose magnitude keeps decaying as the particle separation increases in the flow direction. This explains the slow increase in  $\phi$  with increasing  $\Delta r_1$  which is followed by a rapid decrease, a rapid increase, and an eventually decay towards the equilibrium orientation. Overall, the magnitude of the fluctuation was smaller than  $2\delta$ , and thus PIs did not disturb the aligned microstructure of a SAP suspension.

The effect of tumbling impurities in a suspension of SAPs was also studied using dynamic PI simulations of SAP-SAP, SAP-ET, and ET-ET interactions for  $A = 40$  particles (see section S4 of the Supplemental Material [23]). One might expect the long-range  $O(\epsilon)$  velocity disturbance generated by an ET during its tumbling phase [5,34] to induce multiple tumbling events of SAPs. However, our simulations suggest that around 90% of the SAP tumbling events involved mechanical contact between an ET and a SAP. Furthermore, only  $(2 \pm 0.014)\%$  involved two flips during the PI. The average separation between the two particles was  $(0.16 \pm 0.16)$  when  $\phi$  first became larger than  $\delta$ . Physically this means that an ET flowing in a dilute SAP suspension would induce only occasional local tumbling of SAPs, and a cascade of tumbling events would not occur. The tumbling frequency of a SAP was  $(0.098 \pm 0.025)n\chi$ , which was much smaller than the tumbling frequency of the ET, i.e.,  $2\pi/T = 0.045 + O(n^2)$ , for tumbling particle fraction  $\chi \ll 1$  and  $n \ll 1$ . Figure 9(a) shows  $k$  as a function of  $\chi$ , at  $n = 0.1$ . For a given  $n$ ,  $k$  is linear in  $\chi$  and such linear control could help to obtain precise microstructures in a large-scale manufacturing process.

The effect of a bounding wall on SAPs was also captured using SBT [39–41]. A SAP slowly drifts towards the wall and changes its equilibrium orientation with  $h$ , the distance of its center of mass from the wall, as shown in Fig. 9(b). The wall pushes  $\mathbf{p}$  away from  $\mathbf{p}_U$ , thereby retaining flow alignment. One could use fore-aft asymmetric SAPs, which also have a mean drift in the gradient direction [8,9], to get particles close to the walls of the flow channel and systematically deposit them to impart surface properties like scratch or wear resistance to the final component [42,43].

## VI. MULTIPARTICLE INTERACTIONS BETWEEN SAPs

We showed that SAPs retain flow alignment for  $n \ll 1$  where interactions are primarily pairwise in nature. At sufficiently large value of  $n = O(1)$ , multiple particles will simultaneously interact with a SAP. We investigated the changes in the microstructure of SAP suspensions at such concentrations by using periodic box simulations following the procedure previously used for fiber suspensions [36,37,44–46]. We start with a box containing SAPs with isotropic initial orientations and random spatial positions after avoiding all states with contacting and entangled particles. The particles are then allowed to interact till the moments of the orientation vector reach a value that is statistically invariant (section S2 of the Supplemental Material [23] for details). Our simulations indicate that randomly oriented SAPs moved near the equilibrium orientation  $\mathbf{p}_S$  in an  $O(\delta^{-1})$  time as shown by the variation of  $\langle k \rangle_t$ , the value of  $k$  averaged over all particles inside the periodic box, as a function of time,  $t$ , in Fig. 10(a) at  $n = 0.09$ . During the transient phase most SAPs closely follow the trajectory described by Eq. (1) with some deviations induced by mechanical contacts. SAPs eventually wobble around the equilibrium orientation, and the velocity disturbances generated by temporarily tumbling particles are too weak to induce a cascade of tumbling of SAPs, consistent with our PI simulation results. We also simulated other initial conditions where the particle orientation was not isotropic to reach higher particle concentrations and found that the particle orientation vectors also neared the equilibrium orientation after times of  $O(\delta^{-1})$ .

For obtaining the average values of the flow-alignment parameter, all SAPs were initially in an orientation of  $\mathbf{p} = \mathbf{p}_S$ . The variation of the flow-alignment parameter,  $k = (3/2)\langle 1 - p_2^2 \rangle_{MI}$ , with  $n$  is shown in Fig. 10(b), where  $\langle \cdot \rangle_{MI}$  is the value of  $(3/2)\langle 1 - p_2^2 \rangle$  averaged over all particles in the periodic box and averaged over time. The time averaging was carried out until the results reached a statistical steady state which typically took  $O(10^2-10^3)$  nondimensional time (see section S2 of the Supplemental Material [23] for details). The value of  $k$  is consistent with the PI simulation results for  $n < 0.1$ . In the concentration range of  $n < 0.1$ , MIs are mainly hydrodynamic in nature and cause SAPs to wobble around their equilibrium orientation. This behavior is qualitatively similar to wobbling of a weakly Brownian SAP described earlier and the equivalent orientation distribution is shown in Fig. 7(b) with  $n^{-1}$  serving the role of  $Pe$ . For concentrations  $n \geq n^* \approx 0.2$ , MIs are strong enough to cause  $\phi > \delta$  for a significant portion of time but particle contacts restrict free tumbling. The existence of a critical concentration can be understood if the role of MIs is captured through a rotatory diffusivity of order  $n\epsilon^2\delta^2$ , obtained from the PI scaling argument that diffusivity is proportional to the square of the  $O(\epsilon\delta)$  orientational displacement and the  $O(n)$  interaction frequency [5]. A critical concentration  $n^* = \delta\epsilon^{-2}$  would be akin to a critical Péclet number of  $\delta^{-3}$  described earlier for Brownian SAPs. To confirm the existence of this critical concentration, we also performed MI simulations allowing particles to pass through each other by ignoring the contact forces. Values of  $k$  for this artificial scenario were within 10% of values shown in Fig. 10(b) for  $n < 0.1$  and over two orders of magnitude higher for  $n > 0.2$ . This suggests the importance of mechanical contacts for larger values of  $n$ .

## VII. MICROSTRUCTURE AND MATERIAL CONDUCTIVITY

At a given  $n$ ,  $k$  for ETs, shown by the inset in Fig. 10(b), is much larger than  $k$  for SAPs.  $k$  for SAPs was 0.0013 at  $n = 0.09$ , which is much smaller than the corresponding value of 0.19 for ETs. This difference is shown in Fig. 11, where the highly aligned microstructure of SAPs can be

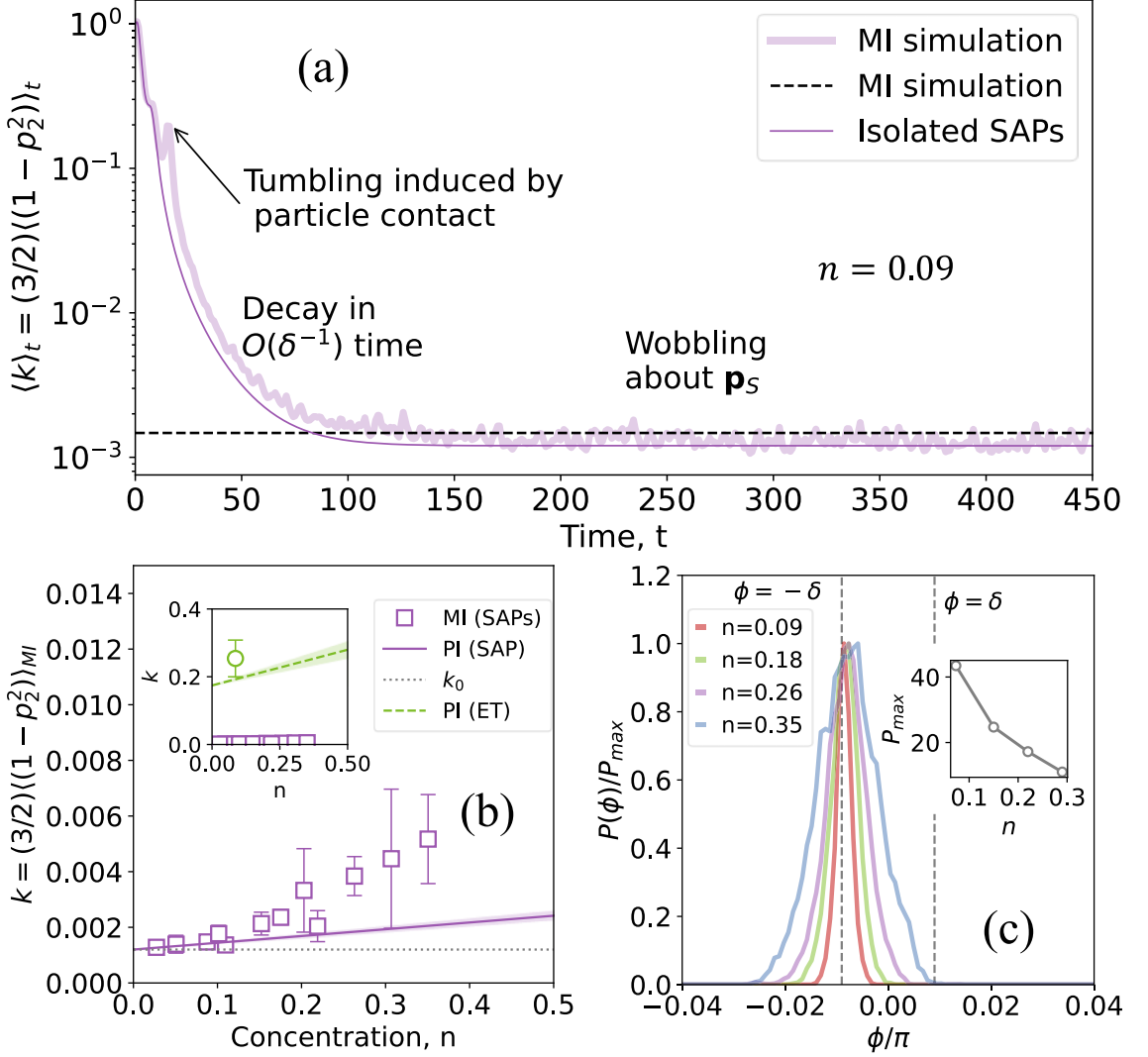
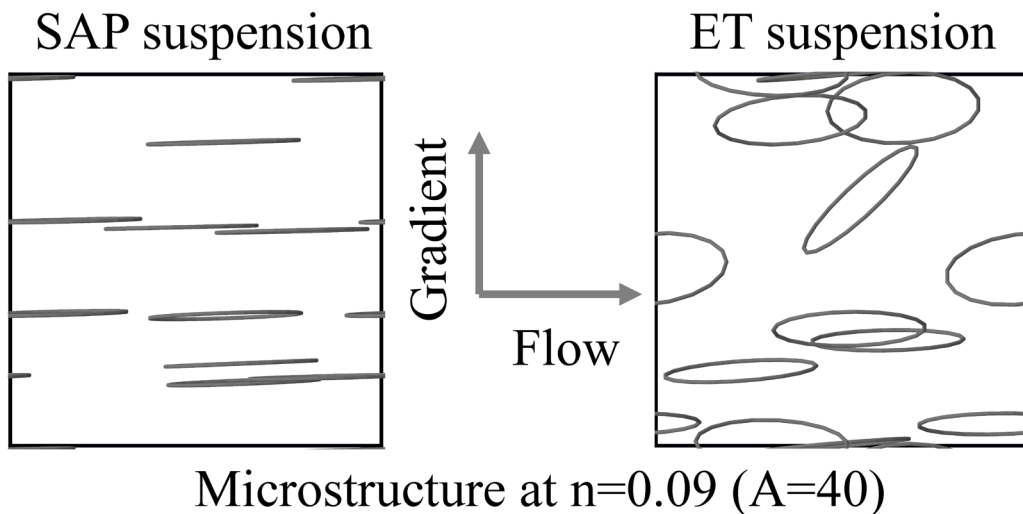


FIG. 10. Multiparticle interactions (MIs) (a) Variation of  $\langle k \rangle_t$  with time. (b)  $k$  for SAPs using MI ( $\square$ ) and PI ( $\circ$ ) simulations; and  $k$  for ETs from PIs ( $- -$  dashed) and MIs ( $\circ$ ) as a function of  $n$ . Shaded region and errorbars represent 95% confidence intervals. (c)  $P(\phi)$  at various  $n$  for  $A = 40$  SAPs.

visually contrasted by the dispersed microstructure of ETs. For a suspension of ETs to obtain a microstructure of the above SAP suspension requires an ET to have an impractical aspect ratio of 2500 (obtained by extrapolating the scaling for  $k$  in [21]). This demonstrates that the highly aligned microstructures of SAP suspensions, such as the one shown in Fig. 11, are inaccessible to tumbling particle suspensions.

The aligned microstructure of SAPs can be used to make composite materials with anisotropic material properties such as thermal conductivity. We calculated the thermal conductivity tensor  $\mathbf{K}$  of a composite material of highly conductive aligned rings relative to the conductivity of the base material  $k_f$  using an effective medium theory [47]. The value of  $\mathbf{K}$  is given by

$$\frac{\mathbf{K}}{k_f} = \left(1 + \frac{4\pi^2 n}{A^2}\right) \mathbf{I} + \frac{2\pi^2 n}{\ln(8A) - 2} \left(1 + \frac{1}{2A^2}\right) (\mathbf{I} - \langle \mathbf{pp} \rangle), \quad (7)$$



\*Image extent is  $(-2.43, 2.43)$  in all 3 directions

FIG. 11. Orientational microstructure of  $A = 40$  SAPs and ETs viewed in the flow-gradient plane.

where we have ignored contributions from contacting particles, which is a good approximation at low concentrations. Because of the high degree of alignment in the flow-vorticity plane, we can expect the in-plane conductivity,  $(K_{11} + K_{33})/2$ , to be much larger than the out-of-plane conductivity,  $K_{22}$ . Figure 12(a) shows the in-plane and out-of-plane conductivity values for composites made of  $A = 40$  SAPs as a function of the volume fraction of particles,  $nV_p$ ,  $V_p$  being the nondimensional

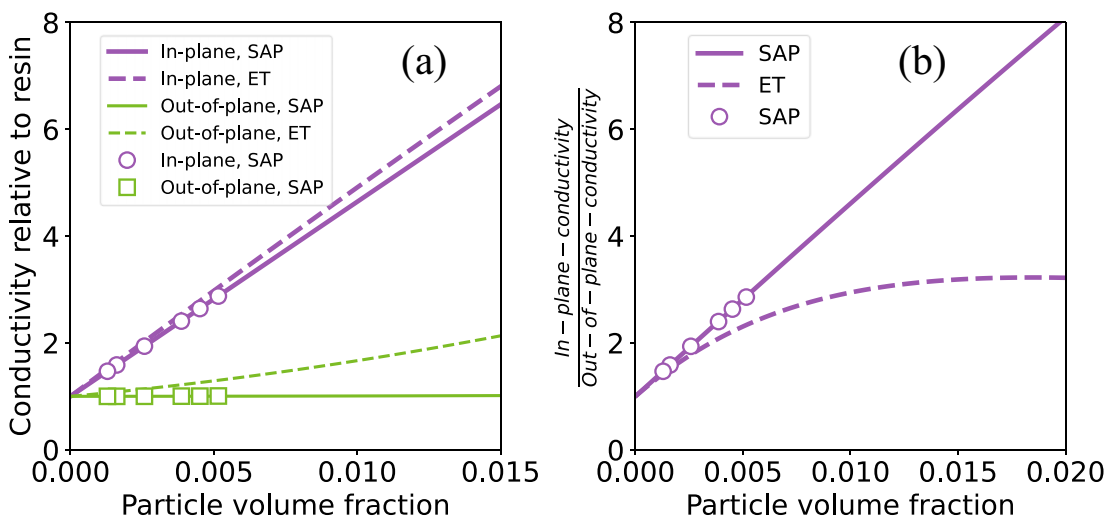


FIG. 12. Conductivity of a composite made of  $A = 40$  SAPs or ETs. (a) Conductivity in the flow vorticity plane (in-plane) and conductivity in the gradient direction (out-of-plane) as a function of the particle volume fraction for SAPs and ETs. (b) Ratio of in-plane and out-of-plane conductivities for a composite of SAPs and ETs. Lines use the average values of the orientational moments from PI simulations, and symbols use the values from MI simulations.



volume of the particle. Thin sheet composites with low conductivity in the thickness, i.e., insulating, and high conductivity in the plane of the sheet can be useful as heat spreader materials. Such composite films can be used between cells of modern day electric vehicle battery packs, providing high thermal conductivity for efficient cooling during normal operations and thermal insulation across the thickness during a thermal runaway event to prevent propagation of heat to adjacent cells [48,49]. The ratio of in-plane and out-of-plane conductivities is shown in Fig. 12(b) as a function of the volume fraction of the particles. Composites made of SAPs will have much higher anisotropy than composites made of ETs as shown in Fig. 12(b).

## VIII. CONCLUSION

In conclusion, our work characterizes the robustness of the microstructure of SAP suspensions to perturbations from Brownian motion, particle interactions, small tumbling impurities, perturbations of the imposed velocity field, or a nearby wall. SAPs influenced by Brownian motion retained their alignment for shear rates greater than  $O[\delta^{-3}(2 - 3\epsilon)k_B\Theta(8\pi^2\mu\epsilon R^3)^{-1}]$ , where  $\Theta$  is the temperature of the suspension,  $\mu$  is the fluid viscosity, and  $k_B$  is the Boltzman constant. At these shear rates, a SAP wobbles around its equilibrium orientation, and the particles remain aligned close to the fluid lamellae. A SAP also wobbled around its equilibrium orientation due to interactions with other particles in the suspension or due to small perturbations to the imposed shear flow. The robust alignment allows SAP suspensions to access highly anisotropic orientational microstructures, such as the one shown in Fig. 11, which are inaccessible to traditional particle geometries (including high-aspect ratio fibers [7,33]). Highly anisotropic materials made from SAP suspensions could include high-conductivity films for flexible electronics [50], or highly porous films for CO<sub>2</sub> capture [51–53] or catalysis [54–56] obtained by solvent evaporation [57].

We also observed that excluded volume interactions become increasingly important to retain the aligned microstructure of SAPs beyond a number density of  $O(\delta\epsilon^{-2})$ . However, the orientational structure of rings at concentrations higher than the ones studied here [ $O(1) < n = O(A)$ ] remains an open question. The microstructure of SAP suspensions at such high concentrations is expected to be influenced by excluded volume interactions similar to disk suspensions [58–61], and there is a possibility of particle jamming. The initial orientation distribution would be dependent on the balance between translational and orientational entropy of the rings for Brownian rings [62], and the initial microstructure would also be strongly dependent on the processing steps used to concentrate the suspension for both non-Brownian and Brownian systems.

The effect of attractive van der Waals forces on SAP microstructure also needs further investigation. Attractive forces between high-aspect ratio rings should be similar to interactions between two thin fibers. The importance of attractive forces could be determined by the ratio of the torque from viscous and adhesive forces on a ring when it is aligned near the flow vorticity plane [63],  $\beta_R = 2\pi^2\mu\gamma R^3|\lambda + 1|/F_a$ , where  $F_a$  is a measure of the adhesive force. The adhesive forces should play a small role when  $\beta_R \gg 1$ , and the microstructure should be well described by the current work. For the case of  $\beta_R \ll 1$ , it is unclear if adhesive forces aid or disturb the aligned microstructure of SAPs. Some of the particle aggregates formed from adhesive contact could also lose their self-alignment property, and the rate of aggregate formation and breakage would also be relevant.

The aforementioned questions could potentially be answered using experiments. Rings can be fabricated using a variety of materials from organic polysaccharides to inorganic colloidal silica using the vortex ring freezing technique [64]. T rings studied here could be fabricated using multistep photolithography [19,20] and tested in a Couette cell with a gap of at least five particle diameters to ignore wall effects and observe alignment for a time that is at least ten times the rotational period of an ET. 3D printed ring-shaped SAPs with triangular cross sections [9] were experimentally observed to sustain permanent alignment compared to a torus that rotated continuously [10]. This is an encouraging result suggesting the possibility of experimentally confirming some of the findings in the present work.

## ACKNOWLEDGMENT

This research was supported by National Science Foundation Grants No. 1435013 and No. 2206851.

- 
- [1] J. M. Dealy and K. F. Wissbrun, *Melt Rheology and Its Role in Plastics Processing: Theory and Applications* (Springer Dordrecht, New York, 2012).
  - [2] F. Lundell, L. D. Söderberg, and P. H. Alfredsson, Fluid mechanics of papermaking, *Annu. Rev. Fluid Mech.* **43**, 195 (2011).
  - [3] G. B. Jeffery, The motion of ellipsoidal particles immersed in a viscous fluid, *Proc. R. Soc. London A* **102**, 161 (1922).
  - [4] F. P. Bretherton, The motion of rigid particles in a shear flow at low Reynolds number, *J. Fluid Mech.* **14**, 284 (1962).
  - [5] M. Rahnama, D. L. Koch, and E. S. Shaqfeh, The effect of hydrodynamic interactions on the orientation distribution in a fiber suspension subject to simple shear flow, *Phys. Fluids* **7**, 487 (1995).
  - [6] D. Fry, B. Langhorst, H. Kim, E. Grulke, H. Wang, and E. K. Hobbie, Anisotropy of sheared carbon-nanotube suspensions, *Phys. Rev. Lett.* **95**, 038304 (2005).
  - [7] K. Yasuda, N. Mori, and K. Nakamura, A new visualization technique for short fibers in a slit flow of fiber suspensions, *Int. J. Eng. Sci.* **40**, 1037 (2002).
  - [8] V. Singh, D. L. Koch, and A. D. Stroock, Rigid ring-shaped particles that align in simple shear flow, *J. Fluid Mech.* **722**, 121 (2013).
  - [9] N. S. Borker, A. D. Stroock, and D. L. Koch, Controlling rotation and migration of rings in a simple shear flow through geometric modifications, *J. Fluid Mech.* **840**, 379 (2018).
  - [10] D. Di Giusto, Ph.D. thesis, Dinamica di fibre in flussi viscosi e turbolenti: uno studio sperimentale e numerico, Universit degli Studi di Udine, 2023, <https://air.uniud.it/handle/11390/1252684>.
  - [11] J. Mansouri, R. Burford, Y. B. Cheng, and L. Hanu, Formation of strong ceramified ash from silicone-based compositions, *J. Mater. Sci.* **40**, 5741 (2005).
  - [12] M. Hassanpour, P. Shafigh, and H. B. Mahmud, Lightweight aggregate concrete fiber reinforcement—A review, *Constr. Build. Mater.* **37**, 452 (2012).
  - [13] A. Yu, P. Ramesh, M. E. Itkis, E. Bekyarova, and R. C. Haddon, Graphite nanoplatelet-epoxy composite thermal interface materials, *J. Phys. Chem. C* **111**, 7565 (2007).
  - [14] A. Y. M. Lin, M. A. Meyers, and K. S. Vecchio, Mechanical properties and structure of *Strombus gigas*, *Tridacna gigas*, and *Haliotis rufescens* sea shells: A comparative study, *Mater. Sci. Eng. C* **26**, 1380 (2006).
  - [15] R. Menig, M. Meyers, M. Meyers, and K. Vecchio, Quasi-static and dynamic mechanical response of *Haliotis rufescens* (abalone) shells, *Acta Mater.* **48**, 2383 (2000).
  - [16] S. De, T. M. Higgins, P. E. Lyons, E. M. Doherty, P. N. Nirmalraj, W. J. Blau, J. J. Boland, and J. N. Coleman, Silver nanowire networks as flexible, transparent, conducting films: Extremely high DC to optical conductivity ratios, *ACS Nano* **3**, 1767 (2009).
  - [17] R. E. Johnson and T. Y. Wu, Hydromechanics of low-Reynolds-number flow. Part 5. Motion of a slender torus, *J. Fluid Mech.* **95**, 263 (1979).
  - [18] N. S. Borker and D. L. Koch, Slender body theory for particles with non-circular cross-sections with application to particle dynamics in shear flows, *J. Fluid Mech.* **877**, 1098 (2019).
  - [19] I. Foulds and M. Parameswaran, A planar self-sacrificial multilayer SU-8-based MEMS process utilizing a UV-blocking layer for the creation of freely moving parts, *J. Micromech. Microeng.* **16**, 2109 (2006).
  - [20] R. Branch, *Two-step photolithography for fabrication of high aspect ratio SU-8 rings*, 2015–2016 Cornell NanoScale Facility Research Accomplishments (2016), pp. 202–203.
  - [21] N. S. Borker and D. L. Koch, Shear rheology of a dilute suspension of thin rings, *J. Rheol.* **67**, 723 (2023).

- [22] L. Leal and E. Hinch, The effect of weak Brownian rotations on particles in shear flow, *J. Fluid Mech.* **46**, 685 (1971).
- [23] See Supplemental Material at <http://link.aps.org/supplemental/10.1103/PhysRevFluids.9.043301> for additional information about the implementation of the numerical simulations and other derivations, which includes Refs. [24–28].
- [24] O. G. Harlen, R. Sundararajakumar, and D. L. Koch, Numerical simulations of a sphere settling through a suspension of neutrally buoyant fibres, *J. Fluid Mech.* **388**, 355 (1999).
- [25] R. Sundararajakumar and D. L. Koch, Structure and properties of sheared fiber suspensions with mechanical contacts, *J. Non-Newtonian Fluid Mech.* **73**, 205 (1997).
- [26] G. Batchelor and J. Green, The determination of the bulk stress in a suspension of spherical particles to order  $c^2$ , *J. Fluid Mech.* **56**, 401 (1972).
- [27] E. Hinch, An averaged-equation approach to particle interactions in a fluid suspension, *J. Fluid Mech.* **83**, 695 (1977).
- [28] H. Hasimoto, On the periodic fundamental solutions of the stokes equations and their application to viscous flow past a cubic array of spheres, *J. Fluid Mech.* **5**, 317 (1959).
- [29] S. H. Strogatz, *Nonlinear Dynamics and Chaos: With Applications to Physics, Biology, Chemistry, and Engineering (2nd ed.)* (CRC Press, 2015).
- [30] R. R. Gabdouliline and R. C. Wade, Brownian dynamics simulation of protein–protein diffusional encounter, *Methods* **14**, 329 (1998).
- [31] S. H. Northrup and H. P. Erickson, Kinetics of protein-protein association explained by Brownian dynamics computer simulation, *Proc. Natl. Acad. Sci. USA* **89**, 3338 (1992).
- [32] H. Brenner, Rheology of a dilute suspension of axisymmetric Brownian particles, *Int. J. Multiphase Flow* **1**, 195 (1974).
- [33] M. P. Petrich, D. L. Koch, and C. Cohen, An experimental determination of the stress–microstructure relationship in semi-concentrated fiber suspensions, *J. Nonnewton. Fluid Mech.* **95**, 101 (2000).
- [34] G. Batchelor, Slender-body theory for particles of arbitrary cross-section in Stokes flow, *J. Fluid Mech.* **44**, 419 (1970).
- [35] M. B. Mackaplow and E. S. Shaqfeh, A numerical study of the rheological properties of suspensions of rigid, non-Brownian fibres, *J. Fluid Mech.* **329**, 155 (1996).
- [36] B. Snook, L. M. Davidson, J. E. Butler, O. Pouliquen, and E. Guazzelli, Normal stress differences in suspensions of rigid fibres, *J. Fluid Mech.* **758**, 486 (2014).
- [37] J. E. Butler and B. Snook, Microstructural dynamics and rheology of suspensions of rigid fibers, *Annu. Rev. Fluid Mech.* **50**, 299 (2018).
- [38] M. v. Smoluchowski, Study of a mathematical theory of the coagulation kinetics of colloidal solutions, *Z. Phys. Chem.* **92U**, 129 (1918).
- [39] J. Blake and A. Chwang, Fundamental singularities of viscous flow: Part I: The image systems in the vicinity of a stationary no-slip boundary, *J. Eng. Math.* **8**, 23 (1974).
- [40] S.-M. Yang and L. G. Leal, Particle motion in Stokes flow near a plane fluid–fluid interface. Part 2. Linear shear and axisymmetric straining flows, *J. Fluid Mech.* **149**, 275 (1984).
- [41] J. Dhanasekaran and D. L. Koch, The hydrodynamic lift of a slender, neutrally buoyant fibre in a wall-bounded shear flow at small Reynolds number, *J. Fluid Mech.* **879**, 121 (2019).
- [42] A. de la Isla, W. Brostow, B. Bujard, M. Estevez, J. R. Rodriguez, S. Vargas, and V. M. Castano, Nanohybrid scratch resistant coatings for teeth and bone viscoelasticity manifested in tribology, *Mater. Res. Innovations* **7**, 110 (2003).
- [43] H. Voss and K. Friedrich, On the wear behaviour of short-fibre-reinforced PEEK composites, *Wear* **116**, 1 (1987).
- [44] D. Saintillan, E. Darve, and E. S. Shaqfeh, A smooth particle-mesh Ewald algorithm for Stokes suspension simulations: The sedimentation of fibers, *Phys. Fluids* **17**, 033301 (2005).
- [45] A.-K. Tornberg and M. J. Shelley, Simulating the dynamics and interactions of flexible fibers in Stokes flows, *J. Comput. Phys.* **196**, 8 (2004).
- [46] J. E. Butler and E. S. Shaqfeh, Dynamic simulations of the inhomogeneous sedimentation of rigid fibres, *J. Fluid Mech.* **468**, 205 (2002).

- [47] A. Rocha and A. Acrivos, On the effective thermal conductivity of dilute dispersions: Highly conducting inclusions of arbitrary shape, *Q. J. Mech. Appl. Math.* **26**, 441 (1973).
- [48] X. He, K. Zhang, H. Wang, Y. Zhang, G. Xiao, H. Niu, and Y. Yao, Tailored carbon-based aramid nanofiber nanocomposites with highly anisotropic thermal conductivity and superior mechanical properties for thermal management, *Carbon* **199**, 367 (2022).
- [49] C.-P. Feng, F. Wei, K.-Y. Sun, Y. Wang, H.-B. Lan, H.-J. Shang, F.-Z. Ding, L. Bai, J. Yang, and W. Yang, Emerging flexible thermally conductive films: Mechanism, fabrication, application, *Nano Micro Lett.* **14**, 127 (2022).
- [50] W. Zeng, L. Shu, Q. Li, S. Chen, F. Wang, and X.-M. Tao, Fiber-based wearable electronics: A review of materials, fabrication, devices, and applications, *Adv. Mater.* **26**, 5310 (2014).
- [51] G. Qi, L. Fu, and E. P. Giannelis, Sponges with covalently tethered amines for high-efficiency carbon capture, *Nat. Commun.* **5**, 5796 (2014).
- [52] A. Wittstock, V. Zielasek, J. Biener, C. Friend, and M. Bäumer, Nanoporous gold catalysts for selective gas-phase oxidative coupling of methanol at low temperature, *Science* **327**, 319 (2010).
- [53] Y. Pan, W. J. Paschoalino, S. S. Bayram, A. S. Blum, and J. Mauzeroll, Biosynthesized silver nanorings as a highly efficient and selective electrocatalysts for CO<sub>2</sub> reduction, *Nanoscale* **11**, 18595 (2019).
- [54] C. Chen, Y. Kang, Z. Huo, Z. Zhu, W. Huang, H. L. Xin, J. D. Snyder, D. Li, J. A. Herron, M. Mavrikakis *et al.*, Highly crystalline multimetallic nanoframes with three-dimensional electrocatalytic surfaces, *Science* **343**, 1339 (2014).
- [55] G. Zhang and M. Mastalerz, Organic cage compounds—from shape-persistency to function, *Chem. Soc. Rev.* **43**, 1934 (2014).
- [56] S. Höger, Shape-persistent macrocycles: From molecules to materials, *Chem.—Eur. J.* **10**, 1320 (2004).
- [57] P. Lu and Y. Xia, Maneuvering the internal porosity and surface morphology of electrospun polystyrene yarns by controlling the solvent and relative humidity, *Langmuir* **29**, 7070 (2013).
- [58] A. Brown, S. Clarke, P. Convert, and A. Rennie, Orientational order in concentrated dispersions of plate-like kaolinite particles under shear, *J. Rheol.* **44**, 221 (2000).
- [59] S. Jogun and C. Zukoski, Rheology of dense suspensions of platelike particles, *J. Rheol.* **40**, 1211 (1996).
- [60] S. Jogun and C. Zukoski, Rheology and microstructure of dense suspensions of plate-shaped colloidal particles, *J. Rheol.* **43**, 847 (1999).
- [61] Q. Meng and J. J. Higdon, Large scale dynamic simulation of plate-like particle suspensions. Part I: Non-Brownian simulation, *J. Rheol.* **52**, 1 (2008).
- [62] D. Frenkel, Order through entropy, *Nat. Mater.* **14**, 9 (2015).
- [63] M. Chaouche and D. L. Koch, Rheology of non-Brownian rigid fiber suspensions with adhesive contacts, *J. Rheol.* **45**, 369 (2001).
- [64] D. An, A. Warning, K. G. Yancey, C.-T. Chang, V. R. Kern, A. K. Datta, P. H. Steen, D. Luo, and M. Ma, Mass production of shaped particles through vortex ring freezing, *Nat. Commun.* **7**, 12401 (2016).